Advances in Aircraft and Spacecraft Science, *Vol. 10, No. 5 (2023) 457-471*
https://doi.org/10.12989/aas.2023.10.5.457

Computation of aerodynamic coefficients of a re-entry vehicle at Mach 6

R.C. Mehta*[1] and E. Rathakrishnan[2]

[1]Department of Aeronautical Engineering, Noorul Islam Centre for Higher Education,
Kumaracoil 629180, India
[2]Department of Aerospace Engineering, Indian institute of Technology, Kanpur 208016, India

(Received September 6, 2023, Revised November 23, 2023, Accepted November 28, 2023)

Abstract. The paper evaluates the aerodynamic coefficients on a blunt-nose re-entry capsule with a conical cross-section followed by a cone-flare body. A computer code is developed to solve three-dimensional compressible inviscid equations for flow over a Space Recovery Experiment (SRE) configuration at different flare-cone half-angle at Mach 6 and angle of attack up to 5°, at 1° interval. The surface pressure variation is numerically integrated to obtain the aerodynamic forces and pitching moment. The numerical analysis reveals the influence of flare-cone geometry on the flow characteristics and aerodynamic coefficients. The numerical results agree with wind tunnel results. Increase of cone-flare angle from 25° to 35° results in increase of normal force slope, axial forebody drag, base drag and location of centre of pressure by 62.5%, 56.2% and 33.13%, respectively, from the basic configuration of the SRE of 25°.

Keywords: aerodynamic coefficients; base flow; computational fluid dynamics; hypersonic flow; re-entry vehicle; shock wave

1. Introduction

Hypersonic flow over a blunt-nosed capsule generates a bow shock, which causes high surface pressure, resulting in the development of aerodynamic forces and pitching moment at an angle of attack, AoA. The trajectory of the re-entry capsule depends on the ballistic coefficient, stagnation point heating, aerodynamic coefficients, and longitudinal static stability. They are identified as shallow or steep, lifting and diving. Re-entry capsule, in general, is an uncontrolled capsule. Its static stability and important parameters are decided by the selection of external configuration of re-entry module. Sufficient static margin should be provided by making $X_{CP}>X_{CG}$. Selection of geometric parameters (Otsu 2021) of space capsules is a major task for improving its volumetric efficiency, ballistic coefficient, flight performance and aerodynamic heating for safe and smooth recovery. Shape of re-entry capsules (Mehta 2019a) can be classified as, head-light shape as in the case of Soyuz, a bell shape in the case of Apollo, saucer type in the case of Orbital Experiment (OREX), umbrella shape in the case of Express Recovery of Space system (EXPRESS), Delft Aerospace Recovery Test (DELFT) and SRE module of Indian Space Research Centre.

---

*Corresponding author, Professor, E-mail: drrakhab.mehta@gmail.com

http://www.techno-press.org/?journal=aas&subpage=7 ISSN: 2287-528X (Print), 2287-5271 (Online)

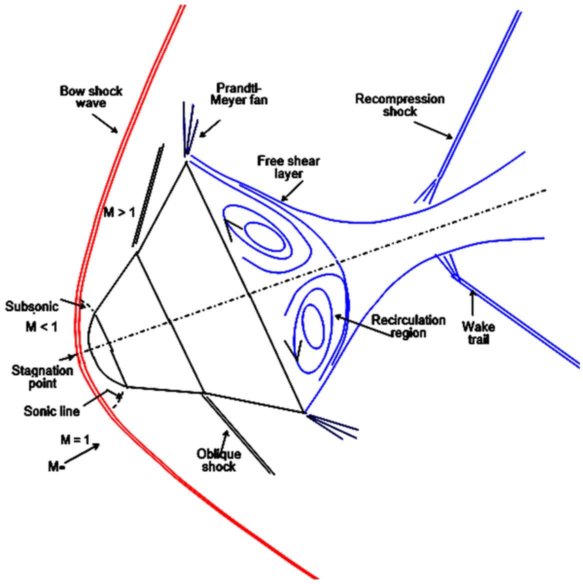

Fig. 1 Schematic sketch of inviscid flow field over SRE at angle of attack

High speed aerodynamics of a blunt-nose body are described by Truitt (1959), Hayes *et al.* (1959). A review of base pressure and base heating of re-entry modules is presented by Lamb *et al.* (1995). Ottens (2001) presented a computational investigation on aerodynamic characteristics of the DELFT capsule. Flow fields over various blunt-nose body modules are numerically evaluated by Viviani and Pezzella (2010a). Computational fluid dynamics (CFD) method is used by Liever *et al.* (2003) to compile aerodynamic data sheets for the Beagle-2 module. Orion Crew Module (OCM) aerodynamic testing has been carried out by Murphy *et al.* (2011). It is important to mention here that a string is required to mount the model in a wind tunnel testing. The presence of sting attachment disturbs the structure of shear layer confluence at the downstream of base region of the module. A conceptual design method has been employed for shape optimization for a space re-entry module by Zhemiz *et al.* (2011). Aerodynamic data of many re-entry modules is compiled by Weiland (2014). Aerothermodynamic characteristics of various space re-entry vehicles are analyzed by Viviani *et al.* (2015b). Numerical simulations of OCM have been carried out by Stremel *et al.* (2011) for various trajectory conditions. Hypersonic flow past a spherically blunted nose-cone body has been analysed to obtain normal density ratio, shock standoff distance, and drag coefficient by Hornung *et al.* (2019). Flow field and aerodynamic characteristics of the Crew Module (CM) at Mach 4 are numerically obtained using FLUENT commercial code by Desikan et al (2015). Hu *et al.* (2017) numerically simulated flow field characteristics of hypersonic flow over a blunt body re-entry module. Aerodynamic force and moment are measured by Laurence *et al.* (2012) on a scale model capsule in a high enthalpy shock tunnel. Inviscid and thin layer Navier-Stokes algorithms are employed to obtain lift, drag, and moment coefficients of Commercial Experiment Transporter (COMET) re-entry vehicle for various Mach number and angle of attack by Wood *et al.* (1996). Dynamic stability of a Mu-Science-Engineering Satellite) MUSES-C re-entry capsule is numerically evaluated at transonic speeds based on Euler and thin layer Navier-Stokes equations by Teramoto *et al.* (2001).

A schematic sketch of inviscid flow field over a Space Recovery Experiment re-entry capsule at an angle of attack is illustrated in Fig. 1. The flow field over capsule depends on external geometry of capsule and freestream conditions. The forebody flow field is dominated by a bow shock wave. A subsonic pocket is imbedded inside a sonic line around the blunt-nose body. The stagnation point lies inside the subsonic region. Away from the stagnation point, the bow shock wave becomes weak due to pressure relief provided by the axisymmetric of the SRE module. Oblique shock wave is formed in the flare-cone junction.

The flow turns around the shoulder of the capsule as shown in Fig. 1. Prandtl-Meyer expansion fan appears on the shoulder of the SRE module and the pressure decreases rapidly. A low-pressure zone is appeared immediately downstream of the base which is characterized by a low-speed recirculating flow region which may be attributed to fill-up of the growing space between the bow shock wave and the module (Mehta 2020b). Hypersonic reentry capsule wake flow field at angle of incidence became asymmetric (Lin *et al.* 2006). Shock wave is formed at this point, called the recompression shock. Beyond the neck is the far field, which extends for many body diameters downstream as the momentum deficit created by the passing capsule is slowly recovered.

The present paper numerically simulates flow field characteristics over various SRE capsules without sting attachment with varying flare-cone half-angle from 25° to 35°, at Mach 6 and angle of attack up to 5° at intervals of 1°. Computed surface pressure distributions over the SRE capsules are numerically integrated to obtain lift, drag, and pitching moment. Numerical results are compared with the available experimental data. The aerodynamic coefficients of the basic model of half-angle 25° are analysed and compared with the other flare-cone model of half-angles 30° and 35°.

2. Numerical analysis

2.1 Governing equations

Three-dimensional compressible inviscid equations are solved in integral form in conjunction with the perfect gas equation of state. The numerically computed flow field simulation contributes to the understanding of flow field and wall pressure distributions over a Space Recovery Experiment re-entry capsule. The governing fluid dynamic equations can be written as

$$\frac{\partial \boldsymbol{U}}{\partial t}+\frac{\partial \boldsymbol{E}}{\partial x}+\frac{\partial \boldsymbol{F}}{\partial y}+\frac{\partial \boldsymbol{G}}{\partial z}=0 \tag{1}$$

The conservative vector can be written as

$$\boldsymbol{U}=[\rho,\rho u,\rho v,\rho w,\rho e]^T \tag{2}$$

The convective flux vectors are not written here but can be found in the texts by MacCormack (2014). The system is closed with equation of state. At M=6, there is insufficient energy to cause dissociation of the gas, therefore perfect gas model is employed, with specific heats ratio γ=1.4, in numerical simulations.

2.2 Numerical algorithm

To facilitate the spatial discretization in the numerical scheme, the governing fluid dynamics

Eq. (1) is written in the integral form inside a computational domain having the computational boundary. The numerical algorithm uses a finite volume discretization technique. The computational domain is divided into several hexahedral cells. The conservative variables $\boldsymbol{U}$ within each cell are calculated from their average values at the cell centre. The convective flux vectors $\boldsymbol{E}$, $\boldsymbol{F}$ and $\boldsymbol{G}$ are computed on each side of the cell. The spatial and temporal terms are decoded using the method of lines. The finite volume code constructed in this way reduces to a central difference scheme and it is second order accurate in space and time, provided the mesh is smooth enough.

The numerical algorithm needs an additional artificial term (Jameson *et al.* 1981) to prevent odd-even decoupling and to control numerical oscillations in the vicinity of severe pressure gradients. Fourth-order dissipation is added everywhere in the flow domain where the solution is smooth but is switched off in the region of shock waves. The term involving the second-order difference is switched on to damp numerical oscillations near the shock waves (Jameson *et al.* 1981). The scheme is stable for a Courant number ≤ 2. Local time steps are used to accelerate a steady state solution by setting the time step at each point to the maximum value allowed by the local Courant-Friedrichs-Lewy stability criterion.

A system of ordinary differential equations in time is obtained after integrating Eq. (1) as described above. Temporal integration is carried out by means of a third-order explicit Runge–Kutta integration algorithm.

2.3 Boundary conditions

At the inlet, wind tunnel test conditions corresponding to M=6 were taken as inflow conditions. An impermeable wall boundary condition has been applied at the solid surface in conjunction with a flow tangency that implies zero convective fluxes across the wall. The surface pressure is calculated from the pressure at the adjacent cell centres.

A far-field boundary condition was considered at a finite distance from the SRE capsule. At an outflow boundary, the two tangential velocity components are extrapolated from the interior.

A half-domain approach was adopted for cases with non-zero angles of attack. A plane of symmetry was used for three-dimensional solutions and circumferential symmetry was employed for axisymmetric solutions.

2.4 Geometry of the SRE

The SRE model is an axisymmetric design. The SRE module consists of a 20° blunt-nosed cone of nose radius R_N=20.42 mm followed by a flare-section with a flare-cone half-angle, θ, that can take values of 25°, 30°, and 35°. Total length of the model is L=57.22 mm. The dimensions of the SRE considered in the analysis are shown in Fig. 2 and Table 1.

2.5 Computational grid

Proper selection of the computational grid is crucial in numerical simulations for capturing the complex flow features such as bow shock, expansion fan, recirculation zones, recompression shock and wake trail region. The grids are well aligned to anticipate these flow features. The computational cells are generated employing finite element method in conjunction with homotopy method (Mehta 2011c). Mono-block, non-overlapping structured grids are generated and then

Table 1 Geometrical variables of SRE module

Model	θ^o	D, mm
M1	25°	73.91
M2	30°	77.89
M3	35°	82.29

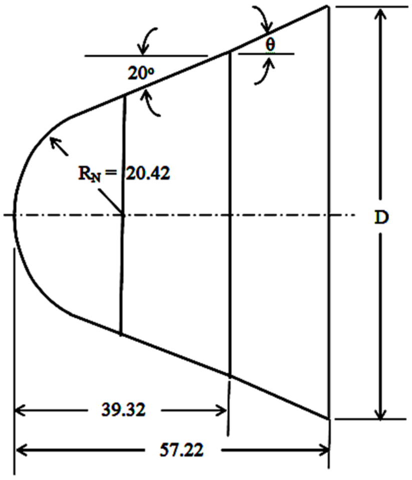

Fig. 2 Dimension of SRE

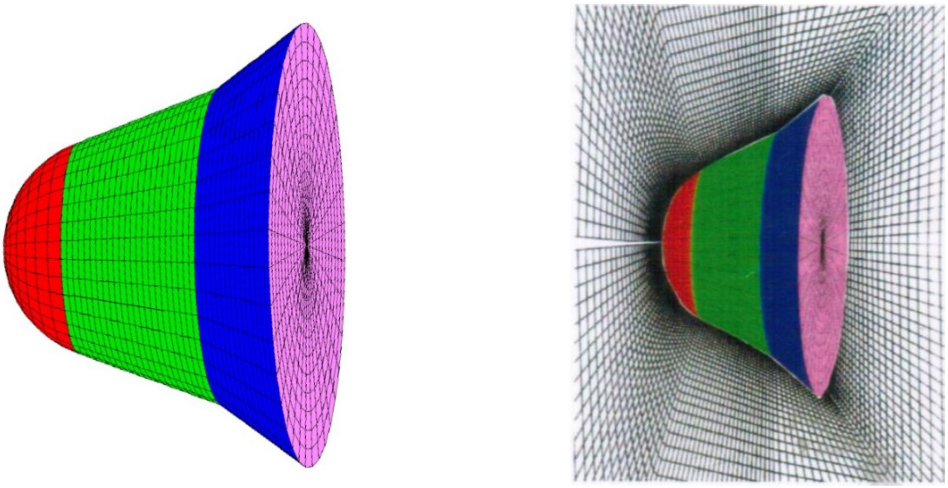

Fig. 3 (a) surface grid (b) 3D grid over SRE

rotated in the azimuthal direction in an orderly manner. The computational domain is having a single-block by joining four connecting computational regions (Mehta 2011c). The grids in the computational domain were composed of hexahedral meshes. The grid has 110 planes axially, 26

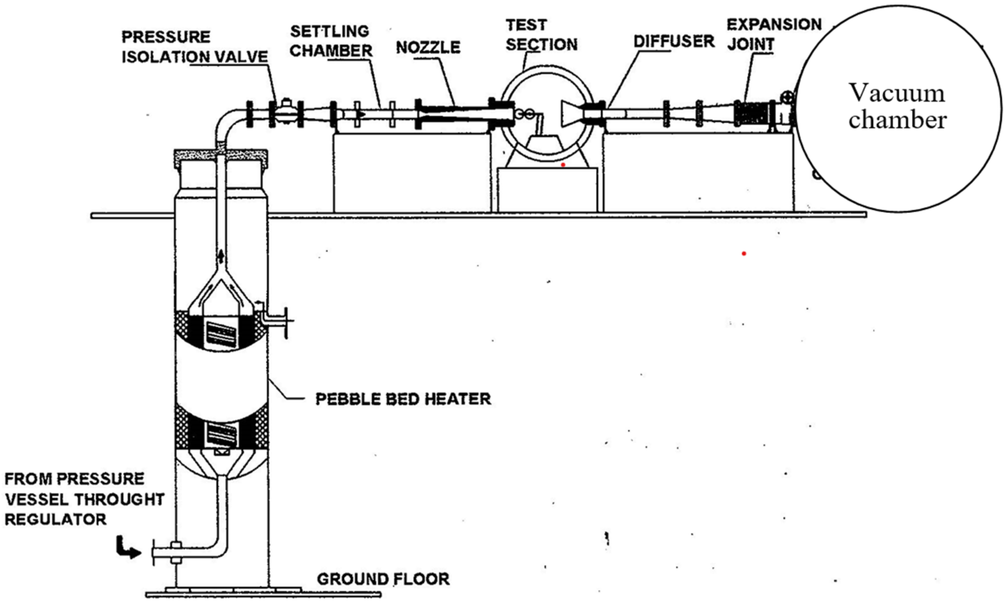

Fig. 4 Schematic diagram of hypersonic wind tunnel

planes circumferentially, and 70 planes normal to the body. The mesh is stretched from the wall to calculate surface pressure. The outer boundary of the computational domain is kept as 1.5−2.5 times the base diameter *D*. In the downstream direction, the computational boundary is about 6-8 times *D*. This grid arrangement is found to yield a relative difference of about ±5% in the computation of fore-body aerodynamic drag coefficient. Fig. 3 (a) and 3(b) depict the surface and symmetry planes of the mesh, respectively. Several grid arrangements are considered to verify the grid's independence. The numerical results are validated with experimental results in the next section.

3. Hypersonic wind tunnel

The hypersonic wind tunnel (Kalimuthu 2009) used for the experiments of this study is an axisymmetric, enclosed free-jet diameter of 25×10^{-2} m. The tunnel system has a high-pressure air supply, a pebble bed heater, contoured nozzles for delivering flow at the required Mach number, a free jet test-section, a fixed geometry diffuser with scoop to collect the nozzle flow and a vacuum system. A schematic diagram of a hypersonic wind tunnel is depicted in Fig. 4. A stainless-steel contoured nozzle of exit diameter of 25.4×10^{-2} m is used to deliver Mach 6 in the test-section. The maximum running time of a wind tunnel is 35 s.

Angle of attack (AoA) of 0 to 5° for these experiments was covered using pitching mechanism. A six-component integral-type strain gauge balance of diameter of 8.0×10^{-3} m was used for force measurement (Kalimuthu 2009). The strain gauge balance can measure normal and axial forces, and pitching moment. The balance is calibrated before the tests. After mounting the model with balance in the test-section, the weight of the model was measured using the calibration matrix through data acquisition mode, with an accuracy of ±1% of actual load, using a normal digital

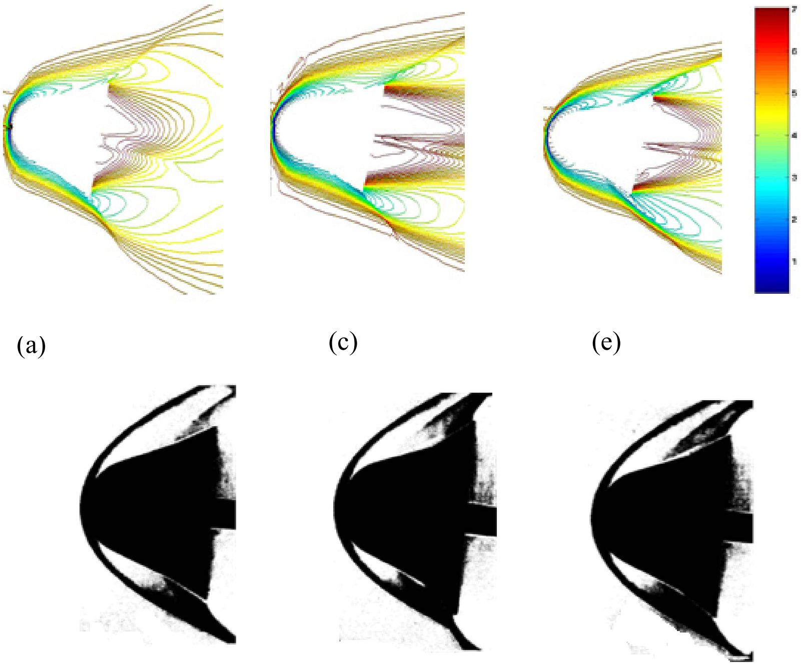

(a) (c) (e)

(b) (d) (f)

Fig. 5 (a) Mach contour, (b) Schlieren pictures at θ=25°, (c) Mach contour, (d) Schlieren pictures at θ=30°, (e) Mach contour, (f) Schlieren pictures at θ=35°, at α=5°

weigh balance. The angle of attack was varied from 0° to 5° in an interval of 1°.

Force measurement data acquisition and processing was carried out by a DAC in a computer. The computer software can control the functions of the ADC and the acquired data is transferred to the computer during the test through a signal conditioner, amplifier, and ADC card. A manual trigger signal from the tunnel control console initiates the data acquisition. This trigger signal also initiates the computer to acquire the data from the total pressure transducer, Pitot pressure transducer, the angle of attack signal from the potentiometer of the pitching mechanism and force measurements data. Data acquisition is terminated when the pitching mechanism reaches *AoA* of 5°. An ADC card in the computer digitizes the analogue signal. Data acquired by the ADC in the computer are subsequently processed separately to get all aerodynamic coefficients.

4. Results and discussion

4.1 Flow field visualization and characteristics

Fig. 5(a)-(f) show the Mach contours in the plane of symmetry and Schlieren pictures over the SRE modules at cone-flare angles θ=25°, 30° and 35° at α=5°. It can be observed from the Mach contours that the flow field in the wake region depends on the cone-flare angle. These flow field

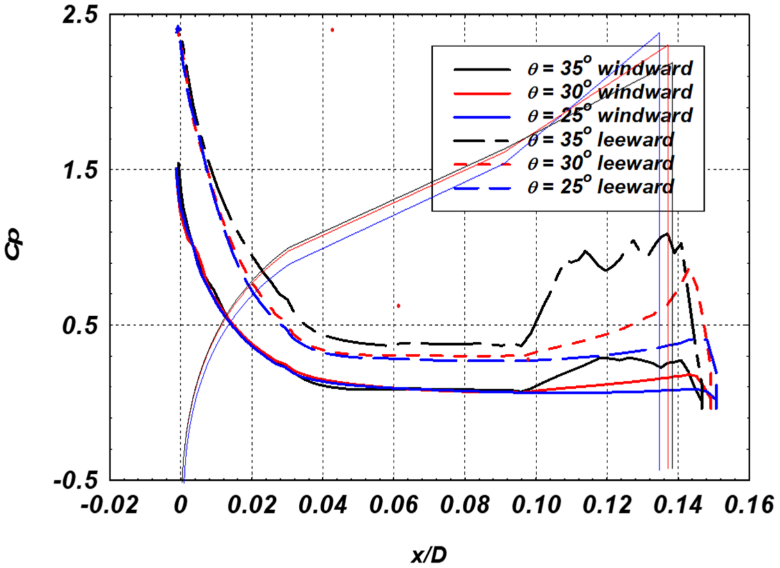

Fig. 6 Variation of surface pressure coefficient over SRE at α=5°

features in Mach contour of Figs. 5(a), 5(c) and 5(e) agree well with the corresponding Schlieren pictures Figs. 5(b), 5(d) and 5(f) of Subramanian *et al.* (1996). The flow field becomes asymmetric due to angle of attack. The flow significantly changed in the windward and the leeward side of the SRE. The flow characteristics depend on the flare half cone angle. The Mach contour captured all the flow field features as seen in the schlieren pictures. The difference in the shock shapes significantly affected the surface pressure distributions and resulted in the aerodynamic forces and pitching moment.

4.2 Surface pressure variations

Fig. 6 shows surface pressure coefficient *Cp* variation over windward and leeward surface of the SRE modules for different values of flare-cone angles at angle of attack α=5°. The x/D=0 represents the stagnation point, where x is the distance measured along the surface from the stagnation point and $D(\theta)$ is the maximum diameter of the SRE model. Variations of *Cp* show differences in the windward and leeward side. Fig. 6 also shows geometry of the SRE with *Cp* to reveal influence of flare-cone angle. The pressure coefficient gradually falls on the sphere-cone region and remains constant over the cone section of the SRE model due to supersonic flow. The surface pressure distribution decreases in the cone-flare section. It can be seen from Fig. 6 the influence of flare-cone angle, θ. There is waviness in the *Cp* variation over the cone-flare of 35° half cone angle due to unsteadiness. To analyse unsteady flow requires solving viscous equations. The purpose of the present numerical analysis is to compute lift, drag, and pitching moment for preliminary design of the SRE using inviscid flow solver. The inviscid analysis will also provide a basic flow field due to change of cone-flare angle. A sudden drop in *Cp* is observed on the shoulder of the module followed by a negative *Cp* variation in the base region. A low pressure is formed immediately downstream of the base which is characterized by a low-speed flow region. In the base region, *Cp* is decreasing with increasing flare-cone angle. Rapid expansion around the

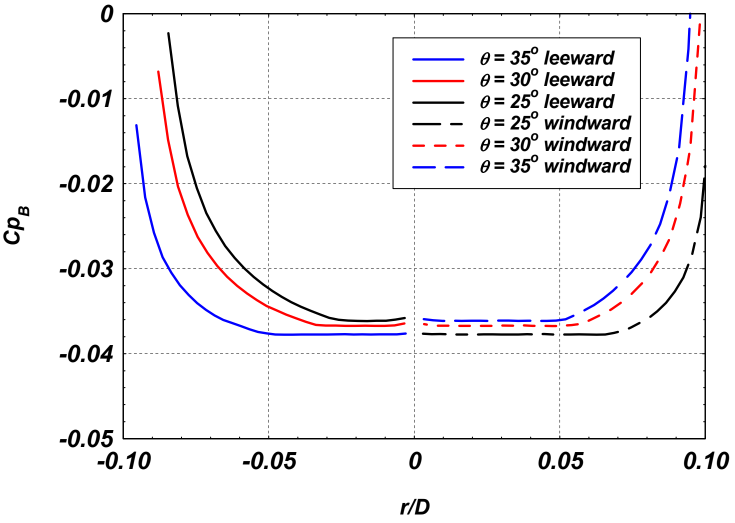

Fig. 7 Variation of radial pressure coefficient on the base of SRE at α=5°

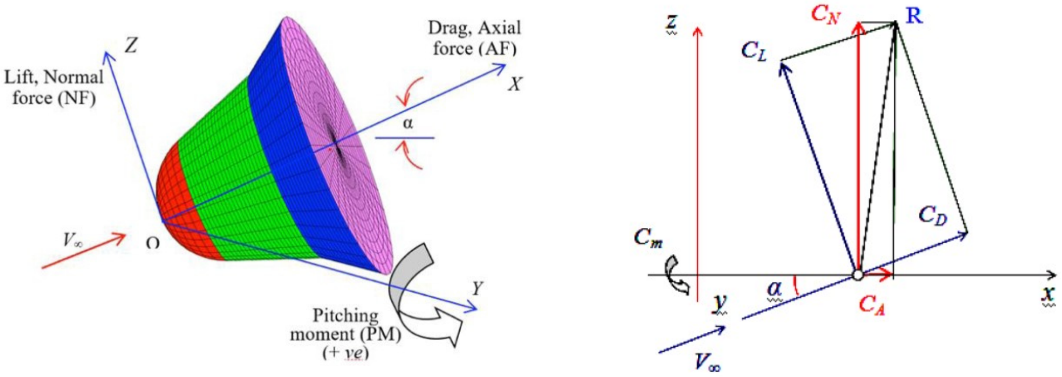

(a) (b)

Fig. 8 (a) Nomenclature of forces on capsule (b) Aerodynamic forces

forebody corners produces high Mach numbers in the outer inviscid region of the wake.

Fig. 7 shows the radial base pressure coefficient distributions on the base of the SRE capsule. On the base of the SRE model, the pressure coefficient is decreasing with increasing flare half cone angles. Constant local pressure coefficient is found in the base region from r/D=-0.034 to -0.045. It reveals the formation of a low-pressure region near the base attributed to rapid expansion.

It is important to mention that it is difficult to measure base pressure in the wind tunnel due to the presence of sting attachment. More importantly, the base pressure at the leeward plane is higher than the leeward base wall pressure. These results indicate that there is significant upstream influence from the base flow upon the base flow fields.

The variations of Mach number in the windward and leeward side over the SRE at angle of attack α=5° are shown by (Mehta 2023d). It is observed that the Mach number reaches up to about 7 on the corner point of the SRE. The variations of windward and leeward side Mach number over the base of the SRE at α=5° is also displayed (Mehta 2023d). It is found that the Mach number reaches up to about 5.5 in the base region of the SRE.

4.3 Aerodynamic forces and moment

The *NF* and the *AF* components with sign convection are depicted in Fig. 8. Nomenclatures in the figure represent *AF* along *OX*, drag (opposite to freestream velocity, V_∞), *NF* along *OY* (perpendicular to *OZ*) and Lift (perpendicular to V_∞), *PM* counter clockwise when looking in *OZ* direction, and α counter clockwise from *OX* when looking in *OZ* direction. Body axis aerodynamics coefficients like C_N and C_A are converted to wind axis aerodynamic coefficients of C_L and C_D. The wind axis aerodynamics relation is given below

$$C_A = \frac{AF}{q_\infty S} \tag{3a}$$

$$C_N = \frac{NF}{q_\infty S} \tag{3b}$$

$$C_L = C_A * \cos\alpha + C_N * \sin\alpha \tag{3c}$$

$$C_D = C_N * \cos\alpha - C_A * \sin\alpha \tag{3d}$$

$$C_{PM} = \frac{PM}{q_\infty SL} \tag{3e}$$

Using the computed circumferential surface pressure distribution, the pressure coefficient is evaluated using the following equation

$$Cp = \left[\frac{p(r,\phi,x) - p_\infty}{q_\infty}\right] \tag{4}$$

The pressure distributions in the circumferential and axial directions were integrated to give the normal lift coefficient C_L and upstream distance of the centre of pressure X_{CP}/L. The normal *AF* and axial *NF* forces measured using following equations

$$C_L = \frac{NF}{q_\infty S} = \frac{2\pi r}{S}\int_0^L\int_0^\pi Cp(\phi,x)\cos\phi d\phi dx \tag{5}$$

The $C_{D,F}$ is computed by integrating the pressure distribution using the following equation

$$C_{D,F} = \frac{AF_F}{q_\infty S} = \frac{2\pi r}{S}\int_0^L\int_0^\pi Cp(\phi,x)\sin\phi d\phi dx \tag{6}$$

The $C_{D,B}$ and C_D can be calculated using the following equations

$$C_{D,B} = \frac{AF_B}{q_\infty S} = \frac{2\pi}{S}\int_0^{D/2}\int_0^\pi Cp(r.\phi) r dr d\phi \tag{7}$$

$$C_D = AF = C_{D,F} + C_{D,B} \tag{8}$$

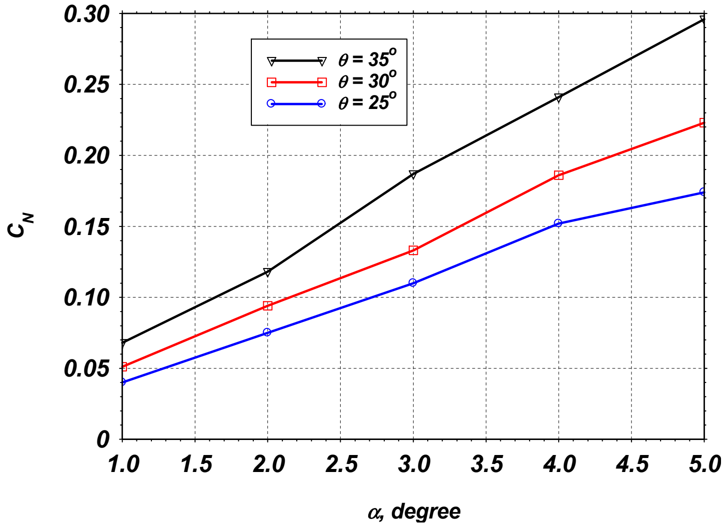

Fig. 9 Variation of C_N with *AoA*

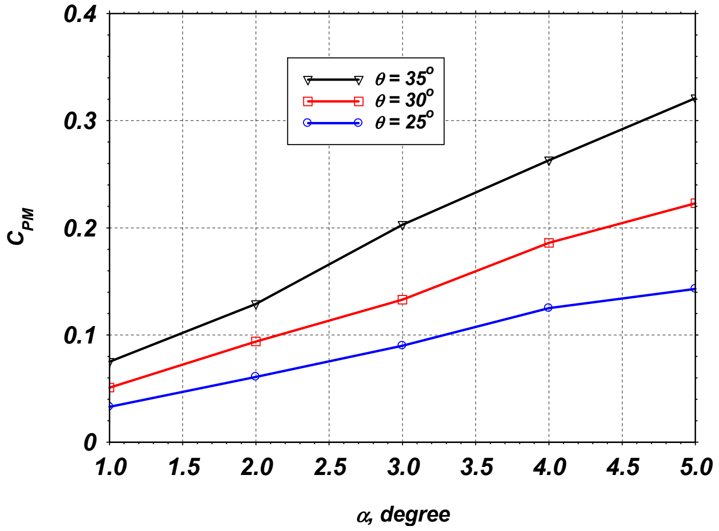

Fig. 10 Variation of C_{PM} with *AoA*

and *PM* and X_{CP} are computed using following equations

$$C_{PM} = \frac{PM}{q_\infty SL} = \frac{2\pi r}{SL}\int_0^L\int_0^\pi Cp(\phi, x)\cos\phi x d\phi dx \tag{9}$$

$$\frac{X_{CP}}{L} = \frac{PM}{NF} = \frac{\int_0^L\int_0^\pi Cp(\phi, x)\cos\phi x d\phi dx}{\int_0^L\int_0^\pi Cp(\phi, x)\cos\phi d\phi dx} \tag{10}$$

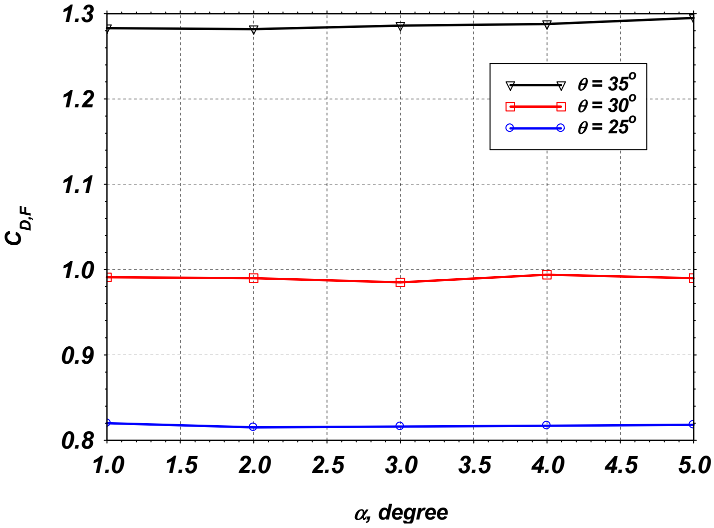

Fig. 11 Variation of $C_{D,F}$ with *AoA*

Table 2 Aerodynamic forces and moment on the SRE capsules

Model	Analysis	$C_{N\alpha}$/deg	$C_{D,F}$	$C_{D,B}$	X_{CP}/L
25° M1	CFD results	0.0364	0.826	-0.065	0.821
30° M2	CFD results	0.0446	0.994	-0.078	0.670
	Difference from 25° M1	22.5%	19.85%	7.9%	13.6%
35° M3	CFD results	0.0591	1.080	-0.080	1.093
	Difference from 25° M1	62.8%	56.2%	7.85%	33.13%

The behaviour of conical bodies shows linear variation with respect to *AoA*. Fig. 9 represents the variation of C_N versus α for the configuration M1, M2, and M3 for (cone half-angle of the flare) 25°, 30° and 35°, respectively. Fig. 10 shows the variation of C_{PM} with α exhibit a similar trend as that of C_N versus *AoA* for all the configurations. The variation of aerodynamic parameters with respect to *AoA* is nearly linear. Fig. 11 shows the variation of $C_{D,F}$ with *AoA* for M1, M2 and M3 configurations.

The variation of aerodynamic coefficients with *AoA* has been obtained by numerically integrating surface pressure coefficients as described above. Table 2 shows computed aerodynamic forces and moment of the different SRE configurations. From the comparisons with wind tunnel data Subramanian *et al.* (1996), we see about 7.85% over prediction in the base drag coefficient and about 13.6% over prediction in the X_{CP}/L. The variation of C_{PM} with α exhibits a linear variation and similar trend as that of $C_{N\alpha}$ for all the configurations. The configuration M2 contributes 22.5% more normal force than M1. Similarly, the configuration M3 which is subjected to larger flow separation contributes 62.8% more normal force than M1. For the capsule M3, the reattachment shock on the windward side gives high pressure downstream of reattachment. This in turn makes the pressure difference between top and bottom sides to be higher and hence C_N is experienced by M2.

For the basic body, the pitching moment shown in this figure is about the nose of the body. The pitching moment of the basic body decreases with increase of angle of attack. In the present analysis, the nose up moment is taken as positive and nose down moment is taken as negative. The pitching moment decreases with increase of angle of attack, almost linearly at all levels of angle of attack. The X_{CP} moves upstream of the nose with angle of attack increase. For the basic body, the X_{CP} moves upstream of the nose with angle of attack increase. The increases in C_{DF} are 19.85% and 56.2% more for configuration M2 and M3 when compared with M1.

4. Conclusions

Flow fields over a spherically blunted body attached with a cone-flare re-entry configuration are numerically computed by solving the three-dimensional compressible inviscid equations for Mach 6 at angle of attack up to 5° at an interval of 1°. Surface pressure coefficient and surface Mach number distributions over the SRE show the influence of the geometrical parameters. Computed Mach contours compare well with the schlieren images. A good agreement is found between calculated aerodynamic coefficients with the available experimental results. The lift and drag coefficients are reduced to 62.8% and 56.2%, respectively, for flare-cone angle 35°. The drag, lift, and pitching moment coefficient is numerically investigated which may be useful for preliminary design as well for static stability margin of the SRE.

References

Desikan, S.L.N., Patil, M.N. and Subramanian, S. (2015), "Understanding of flow features over a typical crew module at Mach 4", *Aeronaut. J.*, **119**, 727-746. https://doi.org/10.1017/S0001924000010794.

Hayes, W.D. and Probstein, R.F. (1959), *Hypersonic Flow Theory*, Academic Press, New York, USA.

Hornung, H., Martinez Schramm, J. and Hannemann, K. (2019), "Hypersonic flow over spherically blunted cone modules for atmospheric entry. Part 1. The sharp cone and the sphere", *J. Fluid Mech.*, **871**, 1097-1116. https://doi.org/10.1017/jfm.2019.342.

Hu. Y., Huang, H. and Zhang, Z. (2017), "Numerical simulation of a hypersonic flow past a blunt body", *Int. J. Numer. Meth. Heat Fluid Flow*, **27**(6), 1351-1364. https://doi.org/10.1108/HFF-05-2016-0187.

Jameson, A., Schmidt, W. and Turkel, E. (1981), "Numerical solution of the Euler equations by finite volume methods using Runge Kutta time stepping schemes", *14th Fluid and Plasma Dynamics Conference*, June.

Kalimuthu, R. (2009), "Experimental investigation of hemispherical nosed cylinder with and without spike in a hypersonic flow", Ph.D. Thesis, Department of Aerospace Engineering, Indian Institute of Technology, Kanpur, India.

Lamb, J.P. and Oberkampf, W.L. (1995), "Review and development of base pressure and base heating correlations in Supersonic flow", *J. Spacecraft Rocket.*, **32**(1), 8-23. https://doi.org/10.2514/3.26569.

Laurence, S.J., Schramm, J.M. and Hannemann, K. (2012), "Force and moment measurements on a free-flying capsule model in a high-enthalpy shock tunnel", *28th Aerodynamic Measurement Technology, Ground Testing, and Flight Testing Conference including the Aerospace T&E Days Forum*, 2861. https://doi.org/10.2514/6.2012-2861.

Liever, P.A., Habchi, S.D., Burnell, S.I. and Lingard, J.S. (2003), "Computational fluid dynamics prediction of the Beagle 2 aerodynamic data base", *J. Spacecraft Rocket.*, **40**(5), 632-638. https://doi.org/10.2514/2.691.

Lin, T.C., Sproul, L.K., Kim, M., Olmos, M. and Feiz, H. (2006), "Hypersonic reentry vehicle wake flow fields at angle of attack", *44th AIAA Aerospace Sciences Meeting and Exhibit*, 582. https://doi.org/10.2514/6.2006-582.

MacCormack, R.W. (2014), *Numerical Computation of Compressible and Viscous Flow*, American Institute of Aeronautics and Astronautics, Inc., USA.

Mehta, R.C. (2013d), "Computational fluid dynamics analysis over a re-entry capsule at Mach 6", *AIAA Scitech 2023 Forum*, 2114. https://doi.org/10.2514/6.2023-2114.

Mehta, R.C. (2017c), "Multi-block structured grid generation for computational fluid dynamics", *Scholar J. Eng. Technol.*, **5**(8), 387-219. https://doi.org/10.21276/sjet.

Mehta, R.C. (2019a), "Numerical simulation of base pressure and drag of space re-entry capsules at high speed, hypersonic vehicles-Past, present and future developments", https://doi.org/10.5772/intechopen.83651.

Mehta, R.C. (2020b), "Computation of base pressure based on to fill-up the growing space applied to reentry capsules", *AIAA Aviation 2020 Forum*, 2711. https://doi.org/10.2514/6.2020-2711.

Murphy, K.J., Bibb, K.L., Brauckmann, G.J., Rhode, M.N., Owens, B., Chan, D.T., Walker, E.L., Bell, J.H. and Wilson, T.M. (2011), "Orion crew module aerodynamic testing", *29th AIAA Applied Aerodynamics Conference*, 3502. https://doi.org/10.2514/6.2011-3502.

Otsu, H. (2021), "Aerodynamic characteristics of re-entry capsules with hyperbolic contours", *Aerosp.*, **8**, 287. https://doi.org/10.3390/aerospace8100287.

Ottens, H.B.A. (2001), "Preliminary computational investigation on aerodynamic phenomena DELFT aerospace re-entry test vehicle*", Proceedings of the 4th European Symposium on Aerothermodynamics for Allocations*, ESA Capua, Italy.

Stremel, P.K., McMullen, M.S. and Garcia, J.A. (2011), "Computational aerodynamic simulations of the Orion command module"*, AIAA Applied Aerodynamics Conference*, 3503. https://doi.org/10.2514/6.2011-3503.

Subramanian, S., Kurup, M.K.A., Kalimuthu R. and Raveendran, P.G. (1996), "An experimental investigation of hypersonic aerodynamic characteristics of re-entry bi-conic configurations at Mach 6", Vikram Sarabhai Space Centre, Trivandrum, India, VSSC/TR/186/96.

Teramoto, S., Hiraki, K. and Fujii, K. (2001), "Numerical analysis of dynamic stability of a reentry capsule at transonic transonic speeds", *AIAA J.*, **39**(4), 646-653. https://doi.org/10.2511/2.1357.

Truitt, R.W. (1959), *Hypersonic Aerodynamic*, Ronald Press, New York, USA.

Viviani, A. and Pezzella, G. (2010a), "Computational flowfield analysis over a blunt-body re-entry vehicle", *J. Spacecraft Rocket.*, **47**(2), 258-270. https://doi.org/10.2514/1.40876.

Viviani, A. and Pezzella, G. (2015b), *Aerodynamic and Aerothermodynamic Analysis of Space Mission Vehicles*, Springer International Publishing A.G., Switzerland.

Weiland, C. (2014), *Aerodynamic Data of Space Vehicles*, Springer-Verlag, Berlin Heidelberg, Germany.

Wood, W.A., Gnoffo, P.A. and Rault, D.F.G. (1996), "Aerothermodynamic analysis of Commercial Experiment Transporter (COMET) re-entry capsule", *34th Aerospace Sciences Meeting and Exhibit*, 316. https://doi.org/10.2514/6.1996-316.

Zhenmiz, Z., Yunliancy, D., Yi, L. and Tieliang, Z. (2011), "Shape optimization design method for the conceptual design of reentry vehicles", *Acta Astonautica Sincia*, **32**(11), 1971-1979.

CC

Nomenclature

AF	axial force
C_A	axial force coefficient
C_D	aerodynamic drag coefficient
C_N	normal force coefficient
C_L	aerodynamic lift coefficient

$C_{L\alpha}$	lift-curve slope
C_{PM}	pitching moment coefficient
$C_{PM\alpha}$	pitching moment coefficient slope
Cp	pressure coefficient
D	base diameter of SRE
$\boldsymbol{E}, \boldsymbol{F}, \boldsymbol{G}$	convective flux vectors
L	length of the SRE
M	Mach number
NF	normal force
PM	pitching moment
p	pressure
q_∞	dynamic pressure
R_N	blunt nose radius
S	reference base surface area
$\boldsymbol{U}$	conservative variable
u, v, w	velocities in the x, y, z directions, respectively
x, y, z	Cartesian coordinate
X_{CG}	location of centre of gravity from nose
X_{CP}	location of centre of pressure from nose
α	angle of attack in pitch plane, AoA
γ	ratio of specific heats
ϕ	circumferential
θ	cone half-angle of the flare
ρ	density

Subscripts

B	base
F	front